The Astronomical Journal, 127:180–198, 2004 January

A DEEP WIDE-FIELD, OPTICAL, AND NEAR-INFRARED CATALOG OF A LARGE AREA AROUND THE HUBBLE DEEP FIELD NORTH[1]

P. Capak,[2] L. L. Cowie,[2] E. M. Hu,[2] A. J. Barger,[2,3,4] M. Dickinson,[5] E. Fernandez,[6] M. Giavalisco,[5] Y. Komiyama,[7] C. Kretchmer,[8] C. McNally,[9] S. Miyazaki,[7] S. Okamura,[10] and D. Stern[11,12]

Received 2003 April 28; accepted 2003 October 8

ABSTRACT

We have conducted a deep multicolor imaging survey of 0.2 deg^2 centered on the Hubble Deep Field North (HDF-N). We shall refer to this region as the Hawaii HDF-N. Deep data were collected in U, B, V, R, I, and z' bands over the central 0.2 deg^2 and in HK' over a smaller region covering the Chandra Deep Field North. The data were reduced to have accurate relative photometry and astrometry across the entire field to facilitate photometric redshifts and spectroscopic follow-up. We have compiled a catalog of 48,858 objects in the central 0.2 deg^2 detected at 5 σ significance in a 3″ aperture in either R or z' band. Number counts and color-magnitude diagrams are presented and shown to be consistent with previous observations. Using color selection we have measured the density of objects at $3 < z < 7$. Our multicolor data indicates that samples selected at $z > 5.5$ using the Lyman break technique suffer from more contamination by low-redshift objects than suggested by previous studies.

Key words: cosmology: observations — galaxies: evolution

1. INTRODUCTION

Deep surveys provide numerous constraints on the structure and evolution of the universe. It has been known that galaxy number counts in a specific bandpass can provide a useful constraint on galaxy evolution (Tinsley 1972; Brown & Tinsley 1974; Tinsley 1980). Multicolor surveys further constrain the galaxy formation history and allow for the selection of galaxies in specific redshift ranges. This work was pioneered in the Hawaii surveys (Cowie 1988) and subsequently used extensively by Steidel et al. (Steidel et al. 1996, 1999) for mapping $z \simeq 3$ and $z \simeq 4$ galaxies. By using a color selection these groups were able to select and obtain spectra for over 1000 $z \simeq 3$ galaxies with a 90% success rate. This gave us a wealth of information about this redshift range. With the ability of modern detectors to take deep images in the near-IR we can now select galaxies up to $z > 6.5$ (Hu et al. 2002). The Hubble Deep Fields (HDFs) (Williams et al. 1996) showed the value of photometric redshifts applied to deep multicolor surveys. This technique allows estimates of redshifts for objects much too faint for optical spectroscopy. It allows for economical measurement of the redshifts of millions of galaxies.

Despite the depth and accuracy of the HDF data, they only cover a small comoving volume. Postman et al. (1998) have looked at the clustering of galaxies using the two-point correlation function of galaxies projected on the sky. This work covered 16 deg^2 in I band. It has shown that galaxies are highly clustered on scales of 15–20 h^{-1} Mpc, where $h = H_0/100$ km s^{-1} Mpc^{-1}. This has provided a challenge in obtaining an unbiased sample of galaxies, since several square degrees must be surveyed. The present paper is the first of a series that will aim to obtain the required data by imaging several 0.2 deg^2 fields.

Previous studies of galaxy formation and evolution have solely used optical data, which introduced biases. However, new generations of radio, X-ray, and mid-IR telescopes have opened up these wavelengths to deep wide-field surveys. X-rays have constrained the active galactic nucleus (AGN) history (Barger et al. 2002), while radio and mid-IR fluxes have proven to be a good probe of star formation. Space-based optical imaging also allowed for the morphological study of galaxies out to high redshift. As such, we have chosen to target regions of the sky that have been observed in multiple wave bands. We began with the HDF-N because of its deep and complete multiwavelength data provided by the Great Observatories Origins Deep Survey (GOODS)[13] and other surveys. We have covered 0.4 deg^2 centered on the Hubble Deep Field North (HDF-N). The central 0.2 deg^2 of these data are of consistent quality in all optical bands; this area contains 48,858 objects detected at 5 σ in R or z' band.

This paper is one in a series focusing on the Hawaii HDF-N. The properties of X-ray–selected objects are discussed in Barger et al. (2003, 2002). Photometric redshifts, spectroscopic redshifts, and multiwavelength analysis will be discussed in

[1] Based in part on data collected at Subaru Telescope, which is operated by the National Astronomical Observatory of Japan.
[2] Institute for Astronomy, University of Hawaii, 2680 Woodlawn Drive, Honolulu, HI 96822.
[3] Department of Physics and Astronomy, University of Hawaii, 2505 Correa Road, Honolulu, HI 96822.
[4] Department of Astronomy, University of Wisconsin–Madison, 475 North Charter Street, Madison, WI 53706.
[5] Space Telescope Science Institute, 3700 San Martin Drive, Baltimore, MD 21218.
[6] New Mexico Institute of Mining and Technology, 801 Leroy Place, Socorro, NM 87801.
[7] Subaru Telescope, 650 North A'ohoku Place, Hilo, Hawaii 96720.
[8] Department of Physics and Astronomy, Johns Hopkins University, 3400 North Charles Street, Baltimore, MD 21218-2686.
[9] Department of Physics and Astronomy, University of Maine, Orono, ME 04469-5709.
[10] Department of Astronomy and Research Center for the Early Universe, School of Science, University of Tokyo, Bunkyo-ku, Tokyo, 113-0033 Japan.
[11] Jet Propulsion Laboratory, Mail Stop 169-327, California Institute of Technology, Pasadena, CA 91109.
[12] Visiting Astronomer, Kitt Peak National Observatory, National Optical Astronomy Observatory, which is operated by the Association of Universities for Research in Astronomy, Inc., under cooperative agreement with the National Science Foundation.

[13] See http://www.stsci.edu/ftp/science/goods.

TABLE 1
TELESCOPES USED, EXPOSURE TIMES, AND DATES OF OBSERVATIONS

Band	Integration Time[a] (hr)	Telescope Used	Typical Integration (s)	Date of Observations
U	28.5	KPNO 4 m	1800	2002 Mar 9–13
B	1.7	Subaru 8.3 m	600	2001 Feb 27, 28
V	6.4	Subaru 8.3 m	1200	2001 Feb 23, 24
	2.0		600	2001 Apr 21–23
R	5.2	Subaru 8.3 m	480	2001 Feb 27, 28
			600	2001 Apr 21–23
I	2.9	Subaru 8.3 m	300	2001 Feb 23, 24
			300	2001 Apr 21–23
			300	2002 Apr 5, 11–14
z′	3.9	Subaru 8.3 m	180	2001 Feb 23, 24, 27, 28
			240	2000 Apr 21–23
HK′	0.43	UH 2.2 m	120	1999–2002

[a] This is the average integration time for a pixel. This varies significantly in the *HK′* image.

Capak et al. (2004). The main focus of the present paper is the optical/IR data reduction and catalog. We also provide number counts and color-color plots to allow for comparison with current and future surveys. We have also selected high-redshift candidates using color selections, and we comment on the effectiveness of this technique at $z > 5$, as well as on the implications for the star formation history.

2. DATA REDUCTION

To optimize our data collection, observations were conducted on a variety of instruments. The *U*-band data were collected using the Kitt Peak National Observatory (KPNO) 4 m telescope with the MOSAIC prime focus camera. This camera has a reasonable *U*-band response and $36' \times 36'$ field of view (Jacoby et al. 1998; Muller et al. 1998; Wolfe et al. 1998). The *B*-, *V*-, *R*-, *I*-, and *z′*-band data were collected using the Subaru 8.2 m telescope and Suprime-Cam instrument (Miyazaki et al. 2002), which is optimized for red optical response and has a $34' \times 27'$ field of view. Finally, our *HK′* data were collected using the QUIRC camera on the University of Hawaii 2.2 m telescope (Hodapp et al. 1996) with a $3.'6 \times 3.'6$ field of view. The *HK′* filter covers both the *H* and *K′* bands in a single filter, which allows for greater depth at the expense of some color information. The details of these observations are found in Tables 1 and 2.

For data collected with Suprime-Cam a five-point X-shaped dither pattern was used with $1'$ steps. The camera was rotated by 90° between dither patterns to remove bleeding from bright stars and provide better photometric calibration. The KPNO 4 m data were collected using a nine-point grid as a dither pattern with $1'$ steps between pointings. For both the Suprime-Cam and KPNO 4 m observations, the telescope was offset by $10''$ in a random direction between dither patterns. The *HK′* data were collected using a 13-point diamond-shaped dither pattern with $10''$ steps between exposures. The filter profiles multiplied by the detector response are plotted in Figure 1, along with the HDF-N filters used in Fernández-Soto et al. (1999). Quantifiable measures of image quality are given in § 2.4.

2.1. *Flat Fielding*

All of these data were reduced using Nick Kaiser's Imcat tools.[14] The *U*, *B*, *V*, *R*, *I*, and *z′* data were first overscan-

[14] See http://www.ifa.hawaii.edu/~kaiser/imcat.

TABLE 2
DATA QUALITY, DEPTH, AND COVERAGE

Band	Seeing (arcsec)	5 σ Limit[a] (AB mag)	Total Area Covered (deg^2)	Deep Area Covered (deg^2)	Date of Observations
U	1.26	27.1	0.40	0.36	2002 Mar 9–13
B	0.71	26.9	0.27	0.20	2001 Feb 27, 28
V	0.71	26.8	0.27	0.20	2001 Feb 23, 24
	1.18		0.40	0.20	2001 Apr 21–23
R	1.11	26.6	0.27	0.20	2001 Feb 27, 28
			0.40	0.20	2001 Apr 21–23
I	0.72	25.6	0.27	0.20	2001 Feb 23, 24
			0.40	0.20	2001 Apr 21–23
			0.40	0.20	2002 Apr 5, 11–14
z′	0.67	25.4	0.27	0.20	2001 Feb 23, 24, 27, 28
			0.40	0.20	2000 Apr 21–23
HK′	0.87	22.1[b]	0.11	0.11	1999–2002

[a] Measured by randomly placing 10^4 $3''$ diameter apertures on an image with detected objects masked out. The apertures were placed at least $3''$ away from the positions of detected objects.
[b] This is the mode of the depth across the field. In a $9' \times 9'$ area around the HDF-N the 5 σ limit is 22.8.

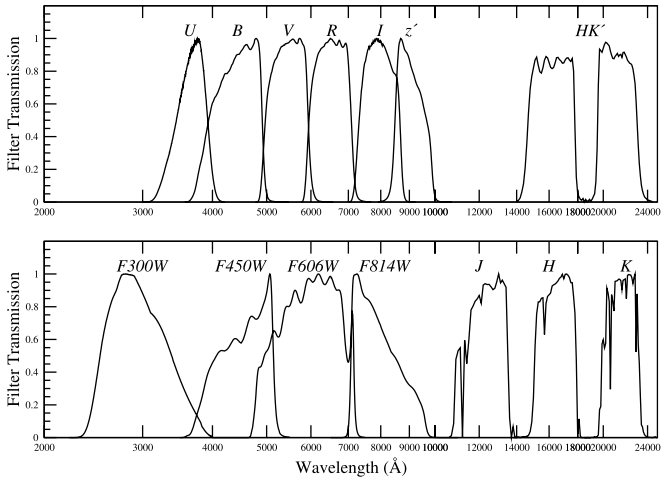

FIG. 1.—Filter profiles multiplied by the quantum efficiency of the detectors used from our survey (*top*) and the HDF-N proper (Fernández-Soto et al. 1999) (*bottom*). All profiles were normalized to have a peak transmission of 1.

corrected and bias-subtracted. Median sky flats were then used to provide a first-pass flat fielding. Objects were then masked out and a second flat field was generated for each dither pattern. The second pass flat fielding was necessary to correct for changes in the instruments due to mechanical flexure and rotation of the camera and optics. The sky was then subtracted using a second-order polynomial surface fit to the sky for each chip of each image. After the first-pass sky subtraction the Suprime-Cam images had time-variable scattered light structure left in the images. This problem occurred at the edges of the field where the camera was vignetted and was worst when the moon was up. To correct for this structure, the objects were masked out and a surface was tessellated to the sky background and subtracted off.

The z'-band data taken before 2001 April were corrected for fringing. To achieve this, a surface was tessellated on a 32 pixel grid over the first-pass flat field. This surface was used to provide first-pass flat fielding instead of the median flat. A median fringe frame was then generated for each night of data, scaled to the background in each image, and subtracted from the flat-fielded images. The images were then second-pass flattened and sky-subtracted, as with the other bands. After 2001 April new chips were installed that had minimal fringing, so fringe subtraction was not performed.

The *U*-band data were corrected for internal pupil reflections, which occur on the MOSAIC camera on the KPNO 4 m telescope. A pupil image was constructed by dividing the *U*-band flat by a *V*-band flat and masking out the areas that did not contain a pupil reflection. The pupil image was subtracted from the *U*-band flat before flat-fielding. The pupil image was then scaled to the background in each image and subtracted off. A second-pass flat fielding was then performed for each dither pattern, as was done for the other bands.

The *HK′* data were collected in 13-point dither patterns, so the data could be flattened and sky subtracted separately for each dither pattern using median sky flats. This allowed us to remove the time variability in the bias, flat field, and sky that occurs in IR arrays. The images in each dither pattern were then combined using a weighted mean to provide an image deep enough to map onto the optical astrometry grid. Cosmic rays were removed during the combination process by looking for pixels that lay more than 5 σ from the weighted mean value. Sigma was calculated from the background noise in each image. Since the image depth varied across the combined, dithered images, an inverse variance map was created for each dither sequence. These inverse variance maps were later used to combine the separate dither sequences.

2.2. *Astrometry*

An initial solution for the optical distortion was calculated by comparing standard star frames with the USNO-A2.0 (Monet et al. 1998). From this point onward we treated each chip in each exposure as a separate image with a separate distortion.

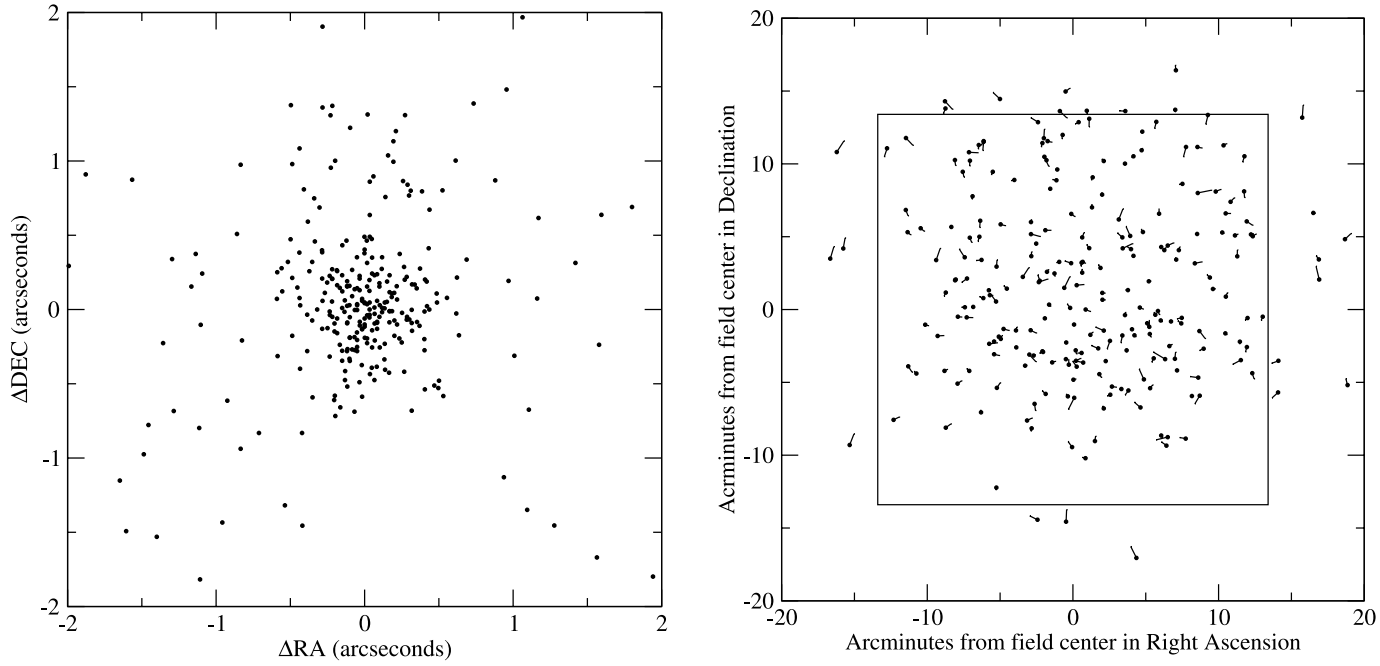

FIG. 2.—Astrometric residuals with respect to the radio catalog of Richards (2000). The inner box on the right-hand side marks the central 0.2 deg^2 in the residual map. The vectors point in the direction of the residual and have and amplitude of 60 times the residual in arcseconds.

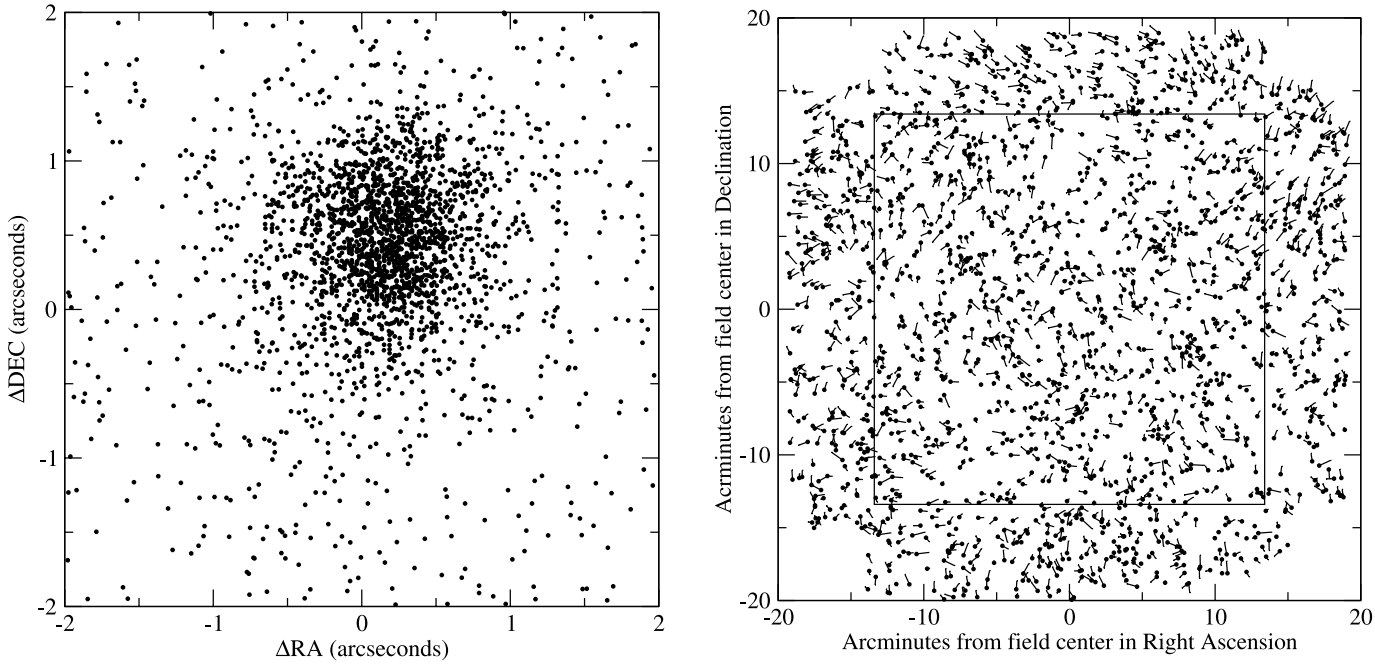

FIG. 3.—Astrometric residuals with respect to the USNO-B1.0 (Monet et al. 2003). The inner box on the right-hand side marks the central 0.2 deg^2 in the residual map. The vectors point in the direction of the residual and have and amplitude of 60 times the residual in arcseconds.

This took into account changes in the optical distortion with time, as well as any mechanical motion on the focal plane.

Using the initial solution, we registered images to one another to cross-identify point sources from image to image. We also identified any USNO-A2.0 (Monet et al. 1998) stars that were not saturated in our images. Since most USNO-A2.0 objects were saturated in the Suprime-Cam images, the MOSAIC *U*-band data were used for the astrometric solution. The *U*-band data were also chosen because they cover a larger area than the other bands.

At magnitudes fainter than 18 the USNO-A2.0 stars are not properly corrected for magnitude-dependent systematics. In addition, errors for individual stars are not quoted in the USNO-A2.0 and are significantly worse than the mean at the faintest level. As such, all USNO-A2.0 stars were assumed to have a root mean square (rms) uncertainty of 2″ in relative astrometry, which is larger than any expected systematics.

In the center of the field USNO-A2.0 stars were only used to constrain the scale factor and absolute astrometry of the fit. The relative astrometry was calculated by minimizing the

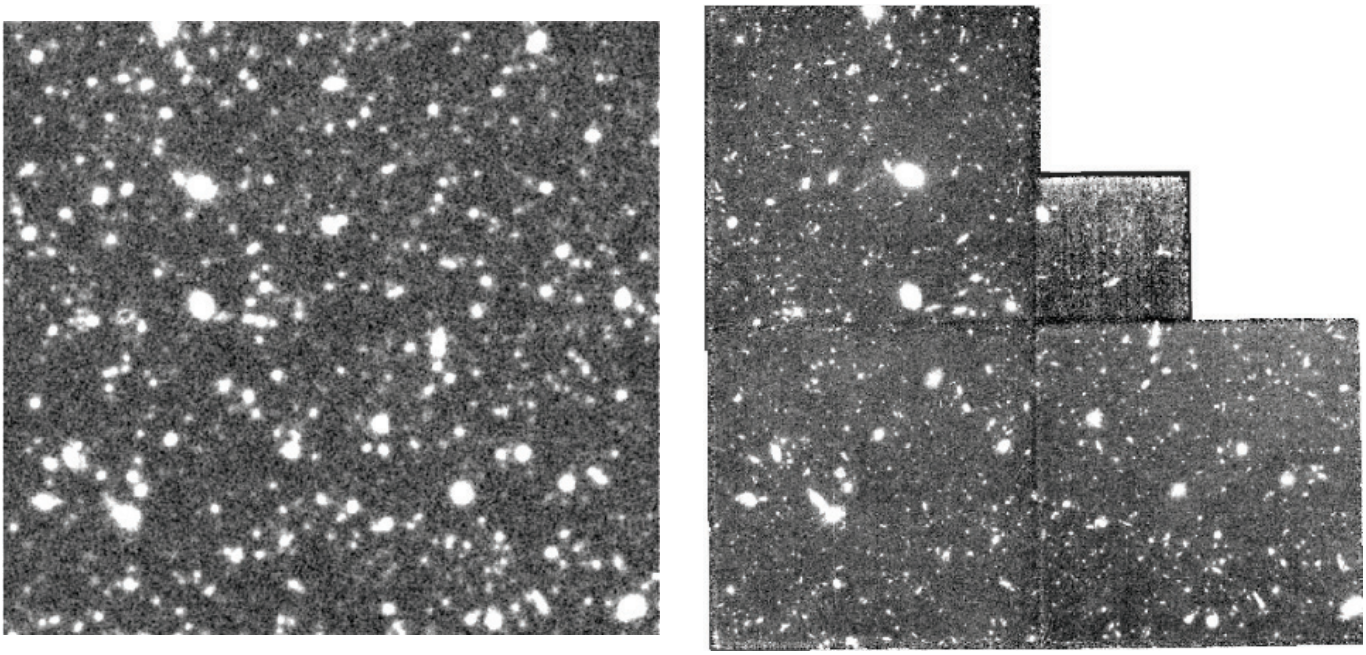

FIG. 4.—On the left is a cutout image of our data around the HDF-N proper in *U* band, and on the right is the *HST* F300W-band image for comparison (Williams et al. 1996). Note the depth and quality of the ground-based image.

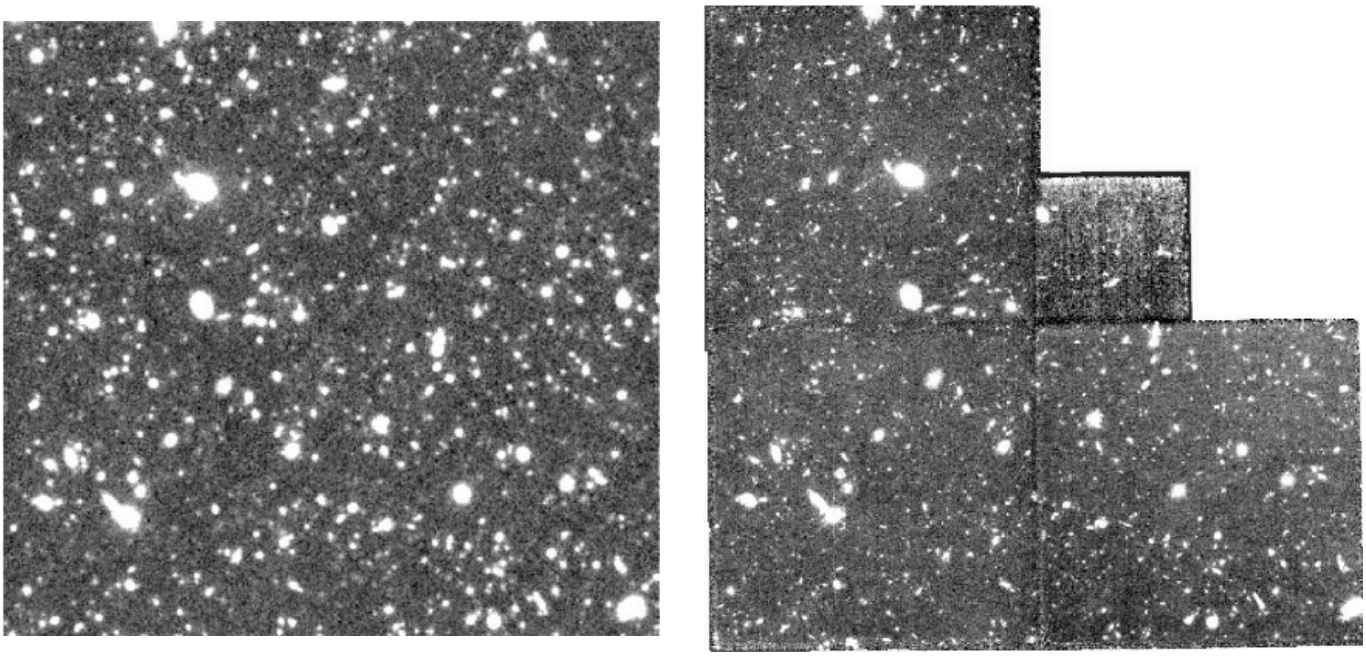

FIG. 5.—On the left is a cutout image of our data around the HDF-N proper in *B* band, and on the right is the *HST* F450W-band image for comparison (Williams et al. 1996). Note the depth and quality of the ground-based image.

positional scatter of stars that appeared in multiple images. This was done by fitting a third-order two-dimensional polynomial to each image. The coefficients of the polynomials were calculated by minimizing the χ^2 defined by equation (1) with respect to the coefficients defined in $f(x, y)$, the polynomial function. In equation (1) N_i is the number of images, and N_s is the number of stars used for the astrometry. In this equation the USNO-A2.0 is treated as an image; however, $f(x, y)$ is replaced with the known star positions. This effectively constrains the scale factor and rotation of the image. Stars that were incorrectly cross-identified between images were removed in an iterative fashion until the astrometric solutions converged:

$$\chi^2 = \sum_{i=0}^{N_i} \sum_{j \neq i}^{N_i} \sum_{s=0}^{N_s} \frac{[f_i(x_s, y_s) - f_j(x_s, y_s)]^2}{\sigma_{i,s}^2 + \sigma_{j,s}^2}. \quad (1)$$

The resulting relative astrometry should be good to the centroiding error of ≈0.1 pixel or ≈0″.03 rms across the

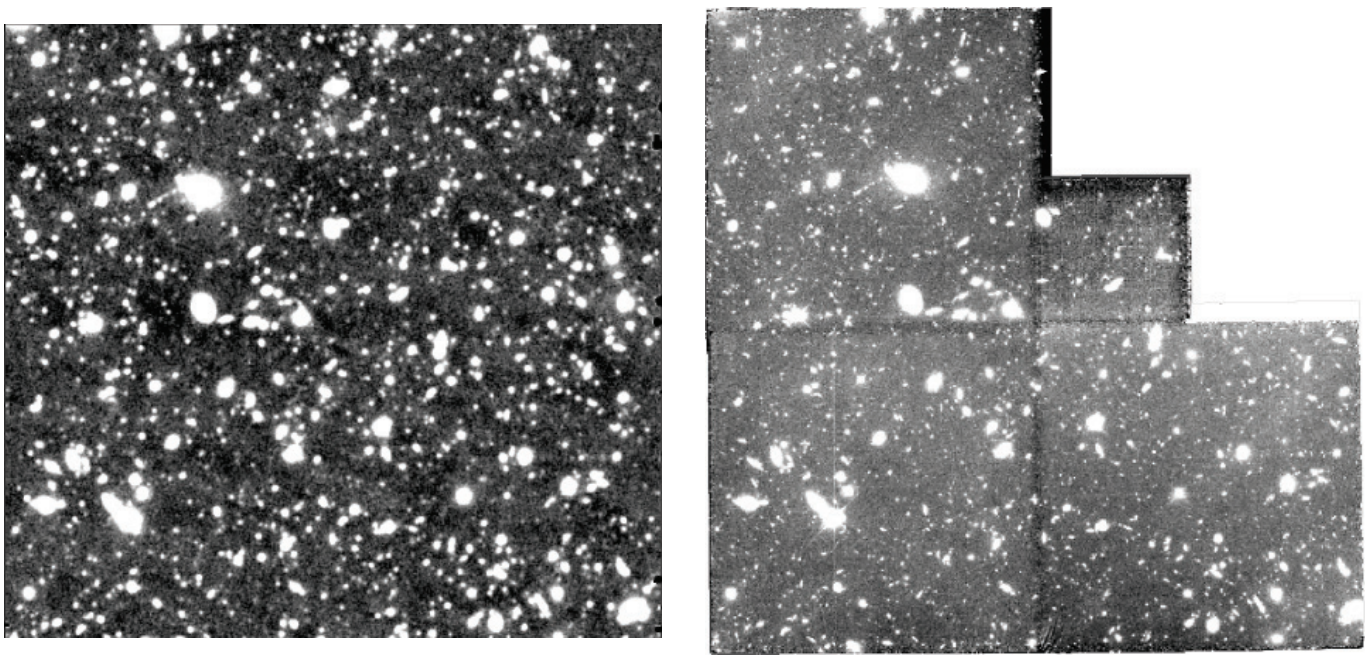

FIG. 6.—On the left is a cutout image of our data around the HDF-N proper in *V* band, and on the right is the *HST* F606W-band image for comparison (Williams et al. 1996). Note the depth and quality of the ground-based image.

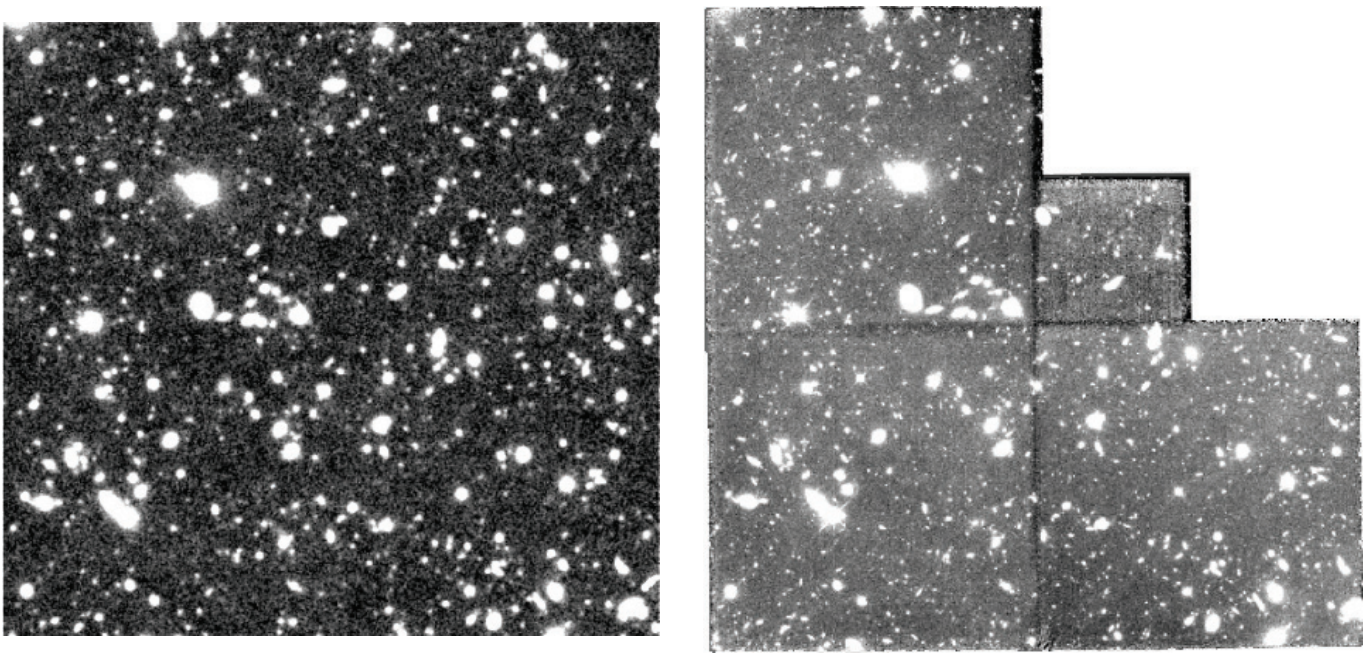

FIG. 7.—On the left is a cutout image of our data around the HDF-N proper in *I* band, and on the right is the *HST* F814W-band image for comparison (Williams et al. 1996). Note the depth and quality of the ground-based image.

center of the field, where there are many measurements for each source. However, this method breaks down at the edge of the field, where there are fewer images. At the very edge of the field the astrometry is only good to 0.″5, since only the USNO-A2.0 constrains the fit; hence, systematics cannot be removed.

Any chromatic aberrations in the astrometry should be minimal, since both the KPNO 4 m and Suprime-Cam have an atmospheric dispersion corrector. A large number of objects with a wide range of colors were used for the astrometry, so any residual effects should be averaged out. A more extensive discussion of this issue can be found in Kaiser (2000).

Once an astrometric grid of objects was established, the *B*, *V*, and *R* data were warped onto it using a two-dimensional, third-order polynomial for each image (still treating each chip separately). To improve the grid in the redder bands, point sources from the astrometrically calibrated *R*-band image were added to the *U*-band astrometric grid. The *I*, z', and HK' data were warped onto this improved grid in the same way as the bluer data. To provide accurate absolute astrometry the final images were registered to the radio catalog of Richards (2000).

We have included comparisons with the radio catalog and USNO-B1.0 (Monet et al. 2003) in Figures 2 and 3. The USNO-B1.0 positions are systematically offset from the radio positions by 0.″5 north and 0.″2 east (see Fig. 3), but this offset was removed before making other comparisons. The rms astrometric scatter between the our positions and the radio positions over the central 0.2 deg^2 field is 0.″22. It is 0.″32 between our positions and the USNO-B1.0. In both cases the scatter is dominated by the astrometric errors in the reference catalogs, which are 0.″16 in the radio catalog and 0.″34 in the USNO-B1.0 and show no systematics across the central 0.2 deg^2 field. As expected we observe systematics with respect to the USNO-B1.0 catalog at the edges of the field; however, these offsets are less than 0.″5 in amplitude. Furthermore systematics at this level are known to exist in the USNO-B1.0 (Monet et al. 2003) so we chose not to remove them.

2.3. *Image Warping and Combination*

For the *U*, *B*, *V*, *R*, *I*, and z' data, chip-to-chip photometric scaling factors were calculated for each dither pattern. This was necessary because each dither pattern was flattened separately, which can change the relative normalization of the chips. When collecting our data, we used large steps in our dither patterns and rotated the camera when possible. This

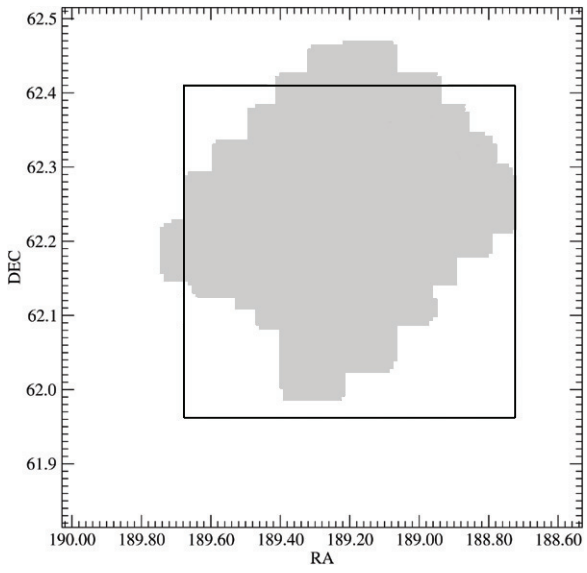

FIG. 8.—The area with HK' coverage is shaded in gray; the catalog area is shown by the black outline. Please note that the HK' data do not cover the whole catalog area.

TABLE 3
PHOTOMETRIC INFORMATION

Band	Zero Point Error[a]	Offsets from SED Fitting	Aperture Correction[b]	Offsets to Vega System[c]	Central Wavelength (Å)	Bandpass (Å)
U	0.031	−0.008	−0.311	0.719	3647.65	387.16
B	0.028	0.000	−0.159	−0.077	4427.60	622.05
V	0.028	−0.005	−0.282	0.023	5471.22	577.36
R	0.026	0.061	−0.262	0.228	6534.16	676.39
I	0.016	0.000	−0.126	0.453	7975.89	792.89
z′	0.018	−0.065	−0.147	0.532	9069.21	802.63
HK′	0.042	−0.181	−0.233	1.595	18947.38	5406.22

[a] Includes the estimated error of 0.01 mag in the Fernández-Soto et al. 1999 catalog.
[b] Used in the calculation of number counts.
[c] Calculated by integrating an A0 star SED multiplied by our filter profile.

meant we could always find a reference chip that covered the same area of sky as two or more chips in another exposure. The scaling between two chips in one exposure could then be calculated by comparing their scaling factors with a chip in another exposure. This was independent of exposure-to-exposure scaling so long as the photometry did not vary across the reference chip. To calculate the scale factors we used 6″ apertures on objects detected at greater than 50 σ with half light radii less than 1.″5. The large apertures were used to prevent any variations in seeing from affecting the scaling. The large number of exposures meant we made many measurements of the chip-to-chip scaling between adjacent chips. These were combined in a weighted mean. Once the chip-to-chip photometric scaling was removed, exposure-to-exposure scale factors were calculated in a similar fashion by comparing overlapping areas between exposures.

The geometric distortions in the MOSAIC and Suprime Cam optics cause each pixel to have a different effective area on the sky. By flat-fielding these images, we introduce a geometry-dependent photometric offset. When calculating the photometric scaling, we corrected for this effect.

The *HK′* data consist of 210 dither patterns of 13 images each. These data were collected under a combination of photometric and nonphotometric conditions. We collected these data in such a way that each dither overlapped several neighboring dither patterns. To correct the photometry, we calculated scale factors for each dither pattern such that the photometric scatter was minimized across the field in the overlapping regions. The absolute zero point was allowed to float during this procedure and later tied to the Fernández-Soto et al. (1999) catalog (see § 2.5).

Saturated pixels were clipped in the *U*-band images before warping or combination. However, saturated pixels in the Suprime-Cam behaved in a very nonlinear fashion, often dropping or ringing in value as they became more saturated. As such, we could not simply clip the saturated pixels. We removed the saturation spikes, along with satellite trails, by searching for strings of elongated objects, which formed straight lines in the images. A strip 21 pixels wide was clipped from the images along detected lines.

After applying photometric corrections, each image was warped onto a stereographic projection. We corrected the geometry-dependent photometric scaling by choosing a mapping that preserved surface brightness. The resampling was done using a nearest-neighbor algorithm. A weighted mean was then calculated for each pixel; pixels that lay more than 5 σ from the mean were rejected to remove cosmic rays. For the *U*, *B*, *V*, *R*, *I*, and *z′* data, the sigma used in the rejection and weighting was measured from the rms background noise in the unwarped image. For the *HK′* images, a sigma was calculated for each pixel during the dither pattern combination and carried through to the final image combination. To avoid clipping pixels that varied due to seeing variations, a window was defined around the median of the pixel values. If a pixel value was between half to twice the median value of all pixels, it was accepted, even if it was more than 5 σ from the mean. A weighted mean and inverse variance were then calculated for all accepted pixels.

The quality of the final images is displayed in Figures 4–7, where we compare cutouts of our data in the HDF-N proper region with the *Hubble Space Telescope* images of Williams et al. (1996) The area with *HK′* data is shown in Figure 8.

2.4. *Object Detection and Measurement*

The catalog of objects was detected in the *R*- and *z′*-band images using SExtractor (Bertin & Arnouts 1996). Objects with three or more pixels rising more than 1.5 σ above the background were analyzed, but only those with 5 σ measurements of their aperture flux were output to the catalog. The significance of a detection was calculated using the rms map generated during the image combination process. The absolute scaling of the rms map was calculated by laying down random blank apertures away from objects on the images. This was done since the pixel-pixel noise underestimates the image noise. This method may somewhat overestimate the true noise since it also includes variations due to faint objects in the blank apertures. The area around bright stars was masked out to prevent erroneous detections and measurements from scattered light.

We calculated both aperture and isophotal magnitudes for our images. Aperture magnitudes were selected as the primary magnitude to avoid biases introduced by galaxy morphology in isophotal magnitudes. To avoid filter dependent aperture corrections the images were smoothed with a Gaussian to match the median ratio of the total to the aperture magnitude in the worst seeing (*U*-band) image. We chose this method because it ensures the apertures are sampling the same percentage of the total light in all bands and does not assume the PSF is Gaussian. PSF matching provided a lower signal to noise because it includes the non-Gaussian components of all seven PSFs, which degraded the image quality. The aperture magnitudes were calculated on these smoothed images while

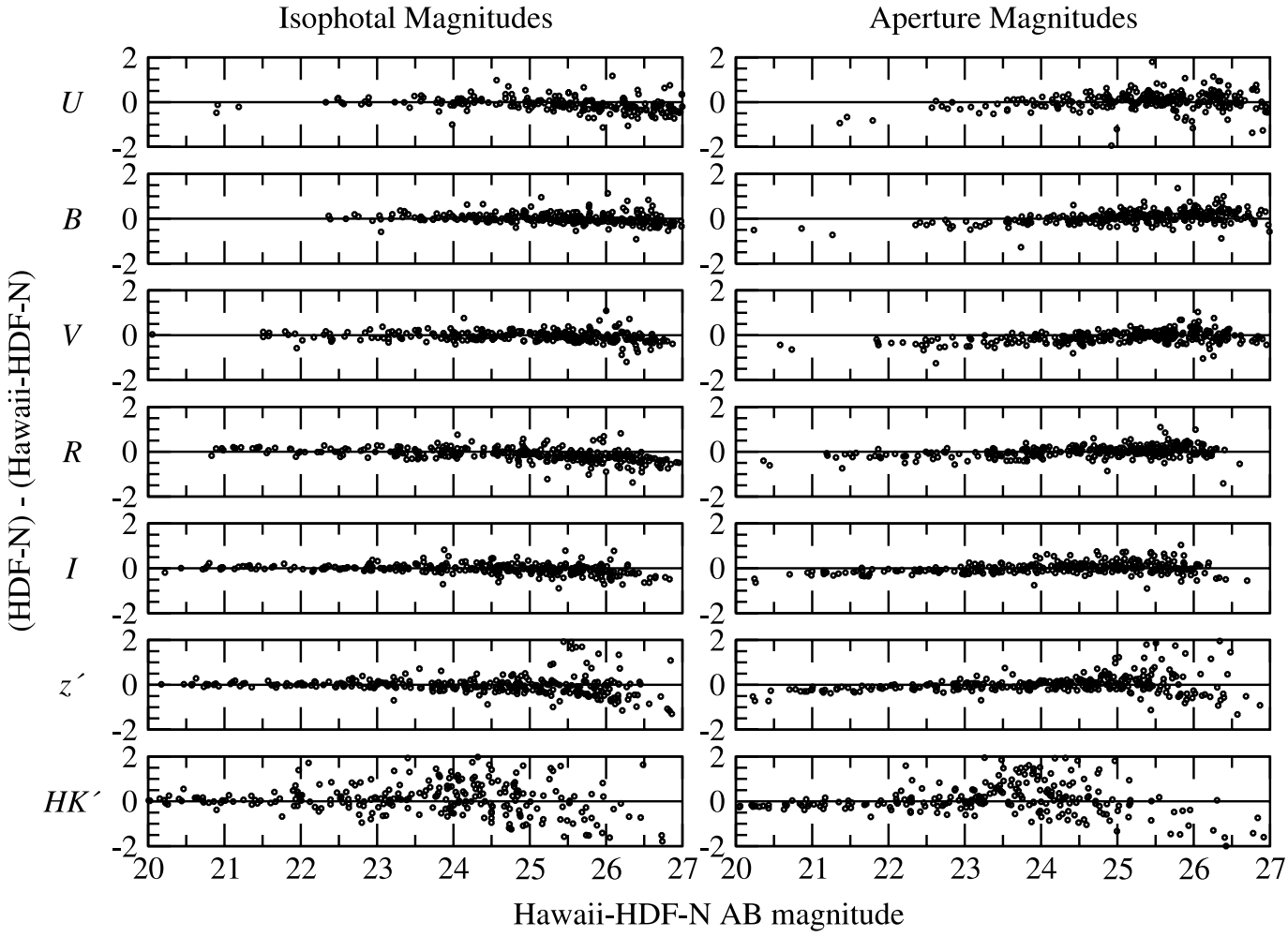

FIG. 9.—Comparison of our photometry with that of Fernández-Soto et al. (1999) from the HDF-N. The magnitudes have been converted to our filter system by linearly interpolating the flux between the HDF-N filters. The rms scatter between our isophotal magnitudes and those of Fernández-Soto et al. is 0.19 mag on average, which corresponds to an average error of 0.03 mag in the zero points.

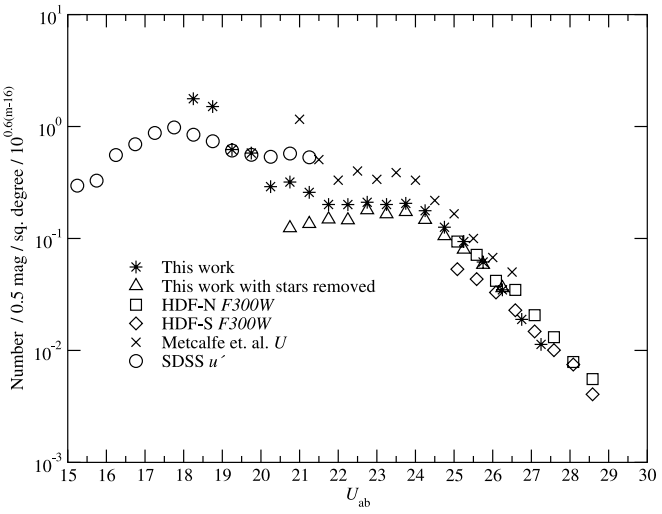

FIG. 10.—*U*-band number counts from this work, the Herschel Deep Field (Metcalfe et al. 2001), the HDF-N (Metcalfe et al. 2001), and the SDSS (Yasuda et al. 2001). Objects were identified as stars if they had a value of 0.9 or greater in the SExtractor star-galaxy separator.

the isophotal magnitudes were calculated on the unsmoothed images. A 3″ diameter aperture was used for the photometry. An annulus with an inner radius of 6″ and outer radius of 12″ was used for sky subtraction. The 5 σ limiting magnitude cut was calculated using aperture magnitudes on the unsmoothed image to avoid losing faint objects.

For the *V*-band data we included archival data to increase the depth (Iwata et al. 2003). These data had better seeing (0.″71 compared with 1.″18); however they did not cover our entire field. Furthermore these data were taken with extremely long exposures which become nonlinear at $\simeq$22nd magnitude To avoid position dependent image quality and saturation, we reduced the archival data separately and scaled them to have matching photometry. Where archival data existed and were unsaturated, they were used for the shape measurements. Photometry was performed on the two images separately and the fluxes combined using a weighted mean.

2.5. *Absolute Photometry*

The HDF-N is a heavily observed area of the sky with extremely accurate photometry in many bands. Many objects have known redshifts and spectral energy distributions (SEDs) making it easy to check the accuracy of our photometry. Furthermore it is difficult to accurately measure standard stars with Suprime-Cam because of the size of the telescope and overheads involved. Obtaining photometry on other telescopes would introduce problems similar to those in using the existing photometry. As such we have chosen not to use standard stars, but rather calibrate the data using the existing photometry.

To obtain accurate absolute photometry in the AB system we matched our photometry to the HDF-N photometry of Fernández-Soto et al. (1999) who carefully corrected for many subtle photometric effects in the HDF-N data. We converted

TABLE 4
CONTENTS OF SHAPE FILE

Column Number	Shape Catalog Item
1	Identification
2	R.A. (J2000.0)
3	Decl. (J2000.0)
4	*x* position on image
5	*y* position on image
6	*U* FWHM[a]
7	*U* semimajor axis[a]
8	*U* semiminor axis[a]
9	*B* FWHM[a]
10	*B* semimajor axis[a]
11	*B* semiminor axis[a]
12	*V* FWHM[a]
13	*V* semimajor axis[a]
14	*V* semiminor axis[a]
15	*R* FWHM[a]
16	*R* semimajor axis[a]
17	*R* semiminor axis[a]
18	*I* FWHM[a]
19	*I* semimajor axis[a]
20	*I* semiminor axis[a]
21	*z′* FWHM[a]
22	*z′* semimajor axis[a]
23	*z′* semiminor axis[a]
24	*HK′* FWHM[a]
25	*HK′* semimajor axis[a]
26	*HK′* semiminor axis[a]

[a] This is the output from the SExtractor FWHM-IMAGE measurement. The FWHM is calculated in a different manner than the semimajor and semiminor axes, which are outputs from the A-IMAGE and B-IMAGE measurements. All three of these measurements were made on the unsmoothed images with respect to centroids in the detection images and have been scaled to arcseconds. A value of zero indicates that the measurement could not be determined. For more information on these parameters see Bertin & Arnouts (1996).

TABLE 5
CONTENTS OF FLAG FILE

Column Number	Flag Catalog Item	Comments
1	Identification	
2	Bad	Set to 1 if the FWHM is 0 in the detecting band
3	U saturated	Set to 1 if any pixel is above saturation the limit
4	B saturated[a]	Set to 1 if $B < 20.49$
5	V saturated[a]	Set to 1 if $V < 19.85$
6	R saturated[a]	Set to 1 if $R < 20.25$
7	I saturated[a]	Set to 1 if $I < 20.15$
8	z' saturated[a]	Set to 1 if $Z < 19.45$
9	HK' saturated	Set to 1 if any pixel is above saturation the limit
10	N overlapping	Number of objects detected within 3″ of this object

[a] Saturated pixels behave in a very nonlinear fashion on Suprime-Cam and can drop in value after reaching the saturation limit. We adopted these magnitude cuts by measuring the magnitude at which point sources became non-Gaussian.

the fluxes in the Fernández-Soto et al. catalog to our filter system by linearly interpolating the flux between the HDF-N filters. The effective wavelength of the filters were used for the interpolation. This method weights by transmission so any overlap between the Fernández-Soto et al. (1999) filters and ours should be accounted for. We then compared our isophotal fluxes to the ones we interpolated and scaled them to match. Since the Fernández-Soto et. al. fluxes were measured in an isophotal aperture, they vary systematically in magnitude with respect to the flux measured in a fixed aperture. To prevent this from introducing filter dependent offsets in our aperture fluxes we used the same magnitude range of 22–24 AB_{mag} in the U, B, V, R, I, and z' bands when comparing our aperture photometry to the Fernández-Soto et. al. photometry. In the

TABLE 6
CONTENTS OF MAGNITUDE FILE

Column Number	Magnitude Catalog Item
1	Identification
2	U aperture magnitude
3	U aperture magnitude error
4	U isophotal magnitude
5	U isophotal magnitude error
6	B aperture magnitude
7	B aperture magnitude error
8	B isophotal magnitude
9	B isophotal magnitude error
10	V aperture magnitude
11	V aperture magnitude error
12	V isophotal magnitude
13	V isophotal magnitude error
14	R aperture magnitude
15	R aperture magnitude error
16	R isophotal magnitude
17	R isophotal magnitude error
18	I aperture magnitude
19	I aperture magnitude error
20	I isophotal Magnitude
21	I isophotal magnitude error
22	z' aperture magnitude
23	z' aperture magnitude error
24	z' isophotal magnitude
25	z' isophotal magnitude error
26	HK' aperture magnitude
27	HK' aperture magnitude error
28	HK' isophotal magnitude
29	HK' isophotal magnitude error

TABLE 7
CONTENTS OF FLUX FILE

Column Number	Flux Catalog Item[a]
1	Identification
2	*U* aperture flux
3	*U* aperture flux error
4	*U* aperture background
5	*U* isophotal flux
6	*U* isophotal flux error
7	*U* isophotal background
8	*B* aperture flux
9	*B* aperture flux error
10	*B* aperture background
11	*B* isophotal flux
12	*B* isophotal flux error
13	*B* isophotal background
14	*V* aperture flux
15	*V* aperture flux error
16	*V* aperture background
17	*V* isophotal flux
18	*V* isophotal flux error
19	*V* isophotal background
20	*R* aperture flux
21	*R* aperture flux error
22	*R* aperture background
23	*R* isophotal flux
24	*R* isophotal flux error
25	*R* isophotal background
26	*I* aperture flux
27	*I* aperture flux error
28	*I* aperture background
29	*I* isophotal flux
30	*I* isophotal flux error
31	*I* isophotal background
32	z' aperture flux
33	z' aperture flux error
34	z' aperture background
35	z' isophotal flux
36	z' isophotal flux error
37	z' isophotal background
38	HK' aperture flux
39	HK' aperture flux error
40	HK' aperture background
41	HK' isophotal flux
42	HK' isophotal flux error
43	HK' isophotal background

[a] All flux values are in nano-Janskys.

HK' band we were forced to use a range of 22–23.5 because of the shallower data. This may have introduced a small bias in our photometry for this band. We then scaled the aperture magnitudes to total magnitudes by comparing our isophotal and aperture fluxes for point sources in the *I* band. *I* band was chosen because it had the best image quality of the red bands and closely approximated the F814W filter used in the HDF-N. To quantify the error in our zero point determination we measured the rms scatter between our isophotal magnitudes and those of Fernández-Soto et. al. The rms scatter is 0.19 mag which corresponds to and average error of 0.03 mag in our photometric zero points exact numbers for all bands are given in Table 3. Figure 9 compares our final photometry to the interpolated photometry of Fernández-Soto et al. (1999).

Since an extensive catalog of spectroscopic redshifts (Cohen et al. 2000) exists for this field it is possible to compare our photometry to galaxy templates. This comparison was done using the photometric redshift code of Benítez (2000) which includes a calibration mode. First a best-fit template at the known redshift was found for each object. The templates of Coleman et al. (1980) and Kinney et al. (1996) were used. Twenty intermediate spectra were interpolated between the main spectral templates to improve the fits. Then a weighed mean offset was calculated for each filter by comparing our photometry to the template photometry. These offsets were then applied to our photometry and the process repeated until the offsets converged. We did not apply offsets the *B* and *I* magnitudes because they are close to the HDF-N F450W and F814W filters respectively and hence we expect them to be correctly calibrated. The resulting offsets are small and are probably due to inaccuracies in the templates or filter profiles (see Table 3). The largest offsets occur in the *R*, z', and HK' bands, which are also those least like the HDF-N filters.

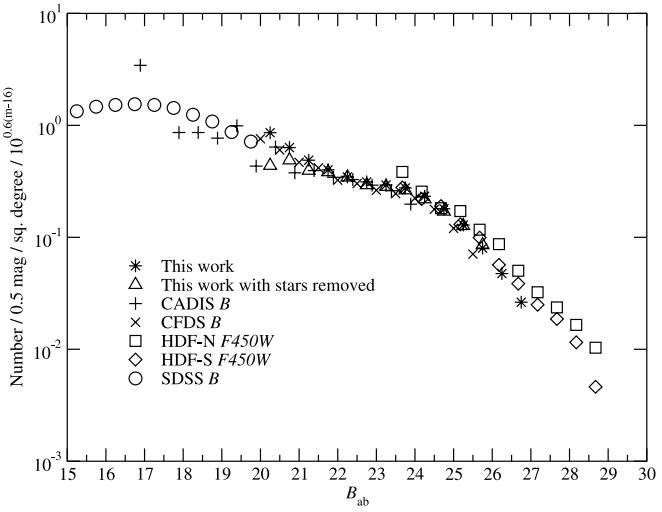

FIG. 11.—*B*-band number counts from this work, the Calar Alto Deep Imaging Survey (CADIS) (Huang et al. 2001), the Canada France Deep Survey (CFDS) (McCracken et al. 2001), the HDF-N (Metcalfe et al. 2001), and the SDSS (Yasuda et al. 2001). Objects were identified as stars if they had a value of 0.9 or greater in the SExtractor star-galaxy separator.

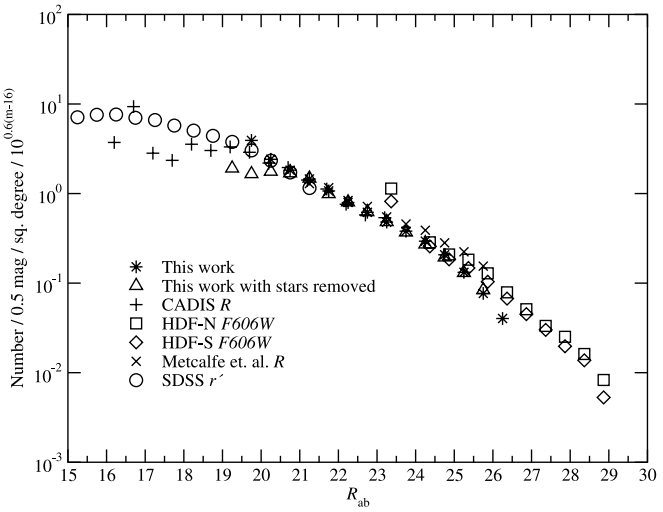

FIG. 13.—*R*-band number counts from this work, the CADIS (Huang et al. 2001), the Herschel Deep Field (Metcalfe et al. 2001), the HDF-N (Metcalfe et al. 2001), and the SDSS (Yasuda et al. 2001). Objects were identified as stars if they had a value of 0.9 or greater in the SExtractor star-galaxy separator.

The large offset in HK' may also be due to the different magnitude range used when scaling the aperture fluxes.

2.6. *Catalog Description*

Because of the large amount of data we have broken the catalog into several files, which are available on the World Wide Web.[15] There are two catalogs, one selected in the R band and the other in the z' band. Objects with an aperture magnitude error smaller than 5 σ on the unsmoothed images in the selecting band were included. If an object was present in both catalogs it was removed from the z' catalog. Each object has a unique identification within each catalog, but both the R and z' catalog begin at 1. Our data cover up to 0.4 deg^2 in some bands, however around the edges the coverage is uneven, the astrometry may be distorted (see § 2.2), and the detections become unreliable due to cosmic rays, reflections, and other defects which could not be removed. As such we avoided these regions for our scientific objectives. All results in this paper are from the central 0.2 deg^2 where the data are of equal depth in the U, B, V, R, I, and z' bands. Since others may find it useful we have included data for the entire field in supplementary files with the same formatting and content as the main catalog. However we strongly recommend using only the main R and z' catalog containing objects in the central 0.2 deg^2. No attempt was made to ensure the integrity of the data outside the central area.

Each catalog consists of four files, the contents of which are listed in Tables 4, 5, 6, and 7. The shape file contains

[15] See http://www.ifa.hawaii.edu/~capak/hdf/index.html.

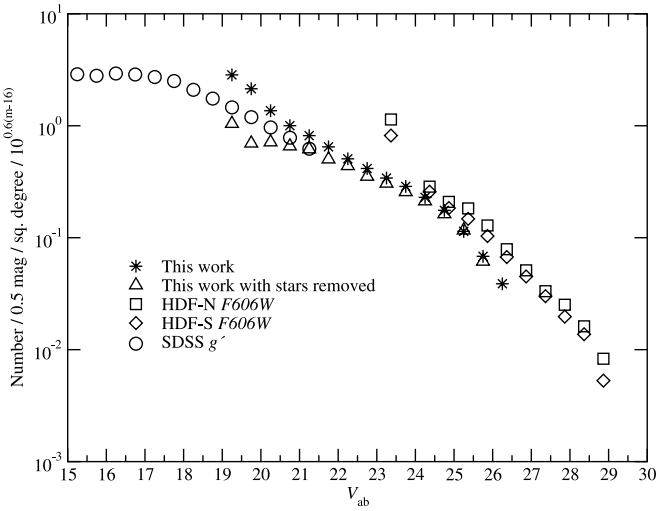

FIG. 12.—*V*-band number counts from this work, the HDF-N (Metcalfe et al. 2001), and the SDSS (Yasuda et al. 2001).

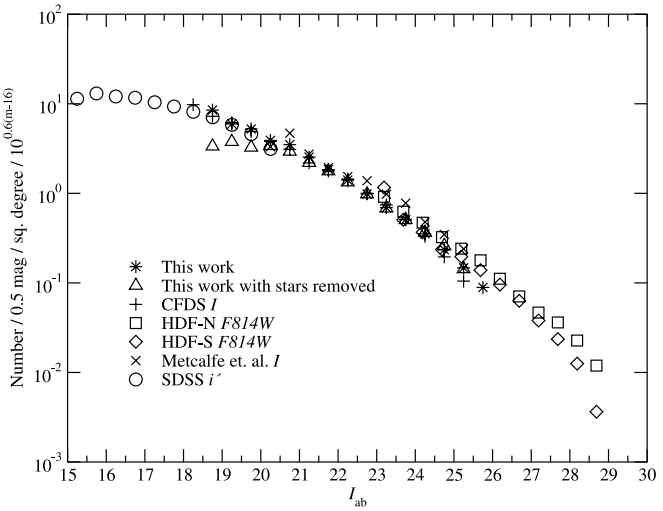

FIG. 14.—*I*-band number counts from this work, the CFDS (McCracken et al. 2001), the Herschel Deep Field (Metcalfe et al. 2001), the HDF-N (Metcalfe et al. 2001), and the SDSS (Yasuda et al. 2001). Objects were identified as stars if they had a value of 0.9 or greater in the SExtractor star-galaxy separator.

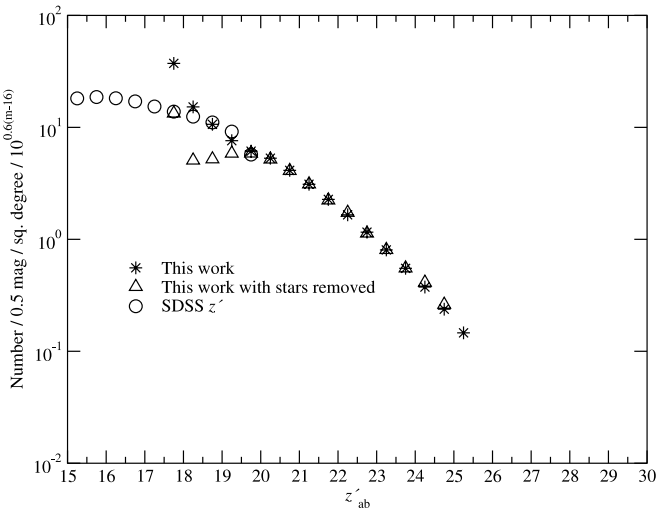

FIG. 15.—The z'-band number counts from this work and the SDSS (Yasuda et al. 2001). Objects were identified as stars if they had a value of 0.9 or greater in the SExtractor star-galaxy separator.

information on the position and morphology of the object output by SExtractor. The flag file contains flags for saturation, overlapping objects, and questionable or bad detections. The bad flag is set for objects with a FWHM of 0 or with abnormal magnitudes in the selection band. This flag was intended to mark questionable detections, however some faint point sources may also have been flagged. The magnitude file contains aperture and isophotal magnitudes along with errors in the AB system for all bands. We used the SExtractor convention of -99 for an object that was outside the field or that could not be measured for other reasons. Badly saturated objects were also given a magnitude of -99. Objects with negative fluxes were assigned negative magnitudes, with the absolute value of the magnitudes corresponding to the absolute value of the flux. The flux

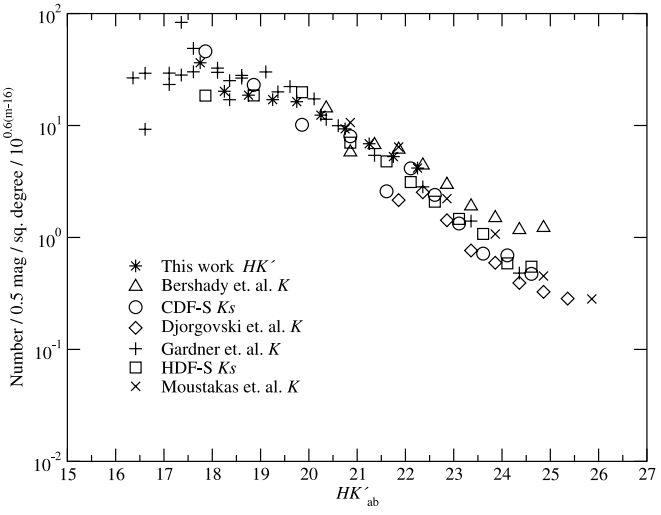

FIG. 16.—K-band number counts from this work, the Chandra Deep Field South (Saracco et al. 2001), the HDF-N (Saracco et al. 2001), and several other authors (Bershady et al. 1998; Moustakas et al. 1997; Djorgovski et al. 1995; Soifer et al. 1994; Gardner et al. 1993) are plotted. An offset of 1.859 was applied to Vega magnitudes to convert them to the AB system.

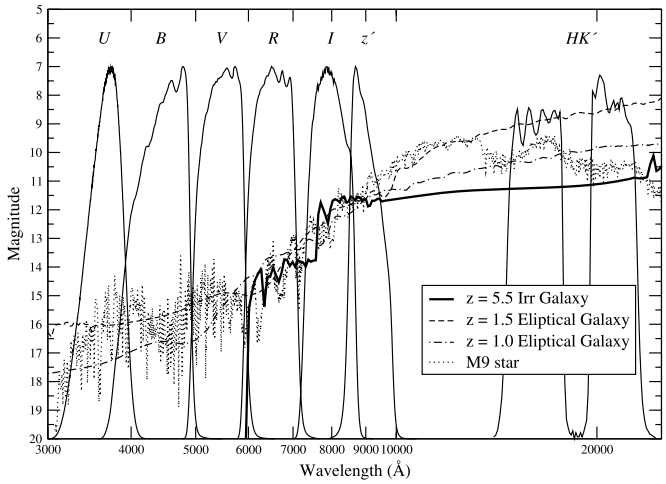

FIG. 17.—Expected SEDs of a $z = 5.5$ star-forming, $z = 1.5$ elliptical, and $z = 1.0$ elliptical galaxy from the Coleman et al. (1980) library shown along with an M9 star from Pickles (1998). These SEDs were corrected for intergalactic absorption using Madau (1995). The filter profiles of our survey are overlaid for comparison. Note the similarity of the SEDs in R, I, and z' bands. Note that differentiating the $z = 5.5$ Irr from the $z = 1.0$ or $z = 1.5$ elliptical requires multicolor information and is most sensitive in the U, B, and near-IR bands. The maximum information comes from the largest wavelength range sample.

catalog contains aperture and isophotal fluxes along with errors and background levels. All measurements in the flux file are in nano-Janskys.

The area around bright objects has been removed because of false detections and problematic photometry in these areas. This was done by cutting out circles around USNO-A2.0 objects with magnitudes brighter than 15.5. A list of these regions and the size of each cutout is provided along with the catalog.

3. RESULTS

3.1. *Number Counts*

To determine number counts, we constructed separate catalogs detected in each color using the unsmoothed images. We measured fluxes in $3''$ diameter apertures and applied an aperture correction to each band. We did not use the SExtractor best or isophotal magnitudes, because they often act in a nonlinear way at low a signal-to-noise ratio. The correction was calculated by measuring the median offset between SExtractor best magnitudes (Bertin & Arnouts 1996), which estimate total magnitudes, and the aperture magnitudes for objects brighter than 24th magnitude (see Table 3). Using aperture magnitudes may introduce a magnitude-dependent bias in the number counts. However, we saw no evidence that the median correction was changing with magnitude. Because of the difficulty in identifying stars at faint magnitudes, we have provided both raw counts and counts with stars removed. Objects were identified as stars if they had a value of 0.9 or greater in the SExtractor star-galaxy separator. We did not remove stars in the HK' band, because the star-galaxy separator was unreliable in that band as a result of variable seeing across the image. The number counts shown in Figures 10–16 were normalized to a Euclidean slope, as described in Yasuda et al. (2001). They agree with those reported by other authors (Metcalfe et al. 2001; McCracken

TABLE 8

FIT OF THE FORM $N = B10^{A(\text{AB MAGNITUDE})}$ TO THE NUMBER COUNTS[a]

Band	Fit Range in AB Magnitudes	A	Error in A	log B	Error in log B
U	20.0–24.5	0.526	0.017	−8.61	0.37
B	20.0–25.5	0.450	0.008	−6.67	0.18
V	20.0–25.0	0.402	0.004	−5.50	0.09
R	20.0–25.0	0.361	0.004	−4.36	0.08
I	20.0–25.0	0.331	0.008	−3.54	0.17
z'	20.0–25.0	0.309	0.006	−2.98	0.13
HK'	16.0–19.0	0.378	0.037	−4.15	0.65
HK'	19.0–22.0	0.393	0.019	−4.31	0.39

[a] N has units of number deg^{-2} 0.5 mag^{-1}.

TABLE 9

RAW NUMBER COUNTS IN N DEG^{-2} 0.5 MAG^{-1}

Magnitude	U	B	V	R	I	z'	HK'
18.25	41 ± 14	...	...	...	...	...	536 ± 70
18.75	46 ± 15	...	...	...	...	454 ± 48	869 ± 89
19.25	77 ± 20	...	...	...	511 ± 51	656 ± 58	1673 ± 124
19.75	98 ± 22	...	346 ± 42	...	914 ± 68	1012 ± 72	2996 ± 166
20.25	103 ± 23	315 ± 40	459 ± 48	852 ± 66	1229 ± 79	1787 ± 96	4632 ± 206
20.75	263 ± 36	485 ± 50	723 ± 61	1265 ± 80	2190 ± 106	2800 ± 120	7148 ± 257
21.25	371 ± 43	712 ± 60	1100 ± 75	2190 ± 106	3259 ± 129	3797 ± 140	12317 ± 337
21.75	557 ± 53	1224 ± 79	1777 ± 95	3048 ± 125	4918 ± 159	6044 ± 176	15655 ± 380
22.25	1048 ± 73	2071 ± 103	2588 ± 115	4551 ± 153	7113 ± 191	8854 ± 213	
22.75	2371 ± 110	3435 ± 133	4282 ± 148	6850 ± 188	10301 ± 230	12135 ± 250	
23.25	4096 ± 145	6468 ± 182	7067 ± 191	10585 ± 233	13984 ± 268	16624 ± 293	
23.75	8389 ± 208	11887 ± 247	11484 ± 243	16268 ± 289	20380 ± 324	22622 ± 341	
24.25	14284 ± 271	19647 ± 318	18727 ± 311	24224 ± 353	29488 ± 390	33802 ± 417	
24.75	19982 ± 321	30361 ± 396	28858 ± 386	35925 ± 430	42827 ± 470	45235 ± 483	
25.25	29824 ± 392	45064 ± 482	40869 ± 459	48474 ± 500	51016 ± 513	44718 ± 480	
25.75	42135 ± 466	60542 ± 559	44073 ± 477	61410 ± 563			
26.25	51093 ± 513	70141 ± 601	27918 ± 379	51863 ± 517			
26.75	39361 ± 450	55831 ± 537					
27.25	21568 ± 333						

TABLE 10

NUMBER COUNTS WITH STARS REMOVED IN N DEG^{-2} 0.5 MAG^{-1}

Magnitude	U	B	V	R	I	z'
18.25	5 ± 5	...	...	...	...	...
18.75	5 ± 5	...	...	...	...	232 ± 34
19.25	5 ± 5	...	...	...	335 ± 41	521 ± 51
19.75	5 ± 5	...	123 ± 25	...	578 ± 54	1043 ± 73
20.25	5 ± 5	154 ± 28	253 ± 36	625 ± 56	1203 ± 78	1839 ± 97
20.75	87 ± 21	346 ± 42	464 ± 49	1198 ± 78	2076 ± 103	2898 ± 122
21.25	191 ± 31	557 ± 53	873 ± 67	2087 ± 103	3104 ± 126	4391 ± 150
21.75	418 ± 46	1079 ± 74	1415 ± 85	2794 ± 120	4990 ± 160	6297 ± 180
22.25	821 ± 65	1932 ± 99	2464 ± 112	4510 ± 152	7501 ± 196	9738 ± 224
22.75	2014 ± 102	3290 ± 130	3952 ± 142	7000 ± 190	10973 ± 238	12688 ± 256
23.25	3699 ± 138	6344 ± 181	6840 ± 187	10823 ± 236	15255 ± 280	18055 ± 305
23.75	7728 ± 199	11784 ± 246	11448 ± 243	16516 ± 292	22617 ± 341	24658 ± 356
24.25	13111 ± 260	19564 ± 317	18918 ± 312	24224 ± 353	32516 ± 409	36705 ± 435
24.75	18737 ± 311	30274 ± 395	28977 ± 386	34618 ± 422	46170 ± 488	46485 ± 490
25.25	28316 ± 382	44956 ± 481	41376 ± 462	46289 ± 489	50778 ± 512	
25.75	41386 ± 462	60434 ± 558	43453 ± 473	59370 ± 553		
26.25	51062 ± 513	69986 ± 601				

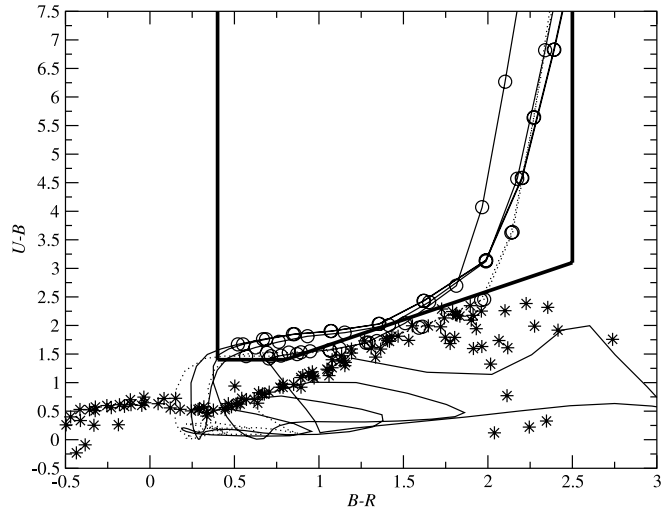

FIG. 18.—$B-R$ vs. $U-B$ color-color plot with galaxy tracks. The region indicated by heavy lines in the top right is where we expect to find $z \simeq 3$ objects similar to those of Steidel et al. (1995). The light solid lines show the expected evolution of Coleman et al. (1980) galaxy templates, and the dotted lines show the Kinney et al. (1996) SB2 and SB3 galaxy templates. The expected colors of stars from Pickles (1998) are overplotted as stars. Circles indicate galaxies in the $2.5 < z < 3.5$ redshift range selected by Steidel et al. (1995).

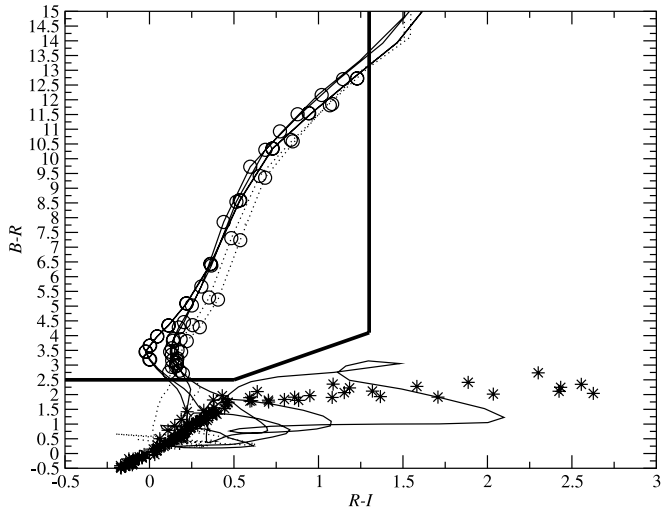

FIG. 20.—$R-I$ vs. $B-R$ color-color plot with galaxy tracks. The region indicated by heavy lines in the top left is where we expect to find $z \simeq 4$ objects similar to those of Steidel et al. (1999). The light solid lines show the expected evolution of Coleman et al. (1980) galaxy templates and the dotted lines show the Kinney et al. (1996) SB2 and SB3 galaxy templates. The expected colors of stars from Pickles (1998) are overplotted as stars. Circles indicate galaxies in the $3.5 < z < 4.8$ redshift range selected by Steidel et al. (1995).

et al. 2001; Huang et al. 2001; Yasuda et al. 2001; Saracco et al. 2001; Djorgovski et al. 1995; Soifer et al. 1994; Gardner et al. 1993). The Sloan Digital Sky Survey (SDSS) counts (Yasuda et al. 2001) were measured in u', g', r', i', and z', which are close to our bands with the exception of g' and r'. The Sloan B-band counts were generated by extrapolating between the u', g', and r' bands (Yasuda et al. 2001). To facilitate comparisons by future authors, we have fitted an exponential of the form $N = B10^{A(\text{magnitude})}$ to our bright end counts, where N is in number per square degree per magnitude. The results of these fits are quoted in Table 8. The number count data are also provided in Tables 9 and 10.

3.2. *Selection of High-Redshift Objects*

High-redshift galaxies have unique colors due to the Lyman break at 912 Å and Lyα absorption blueward of 1216 Å. We can select theses galaxies by choosing three

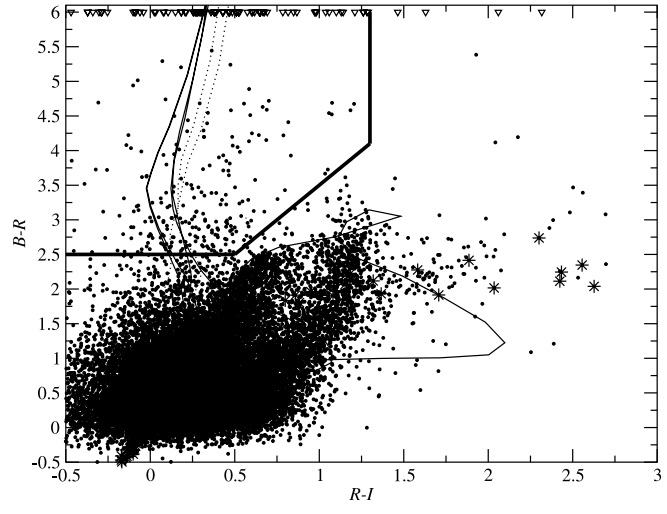

FIG. 19.—$R-I$ vs. $B-R$ color-color plot for all objects with $R_{AB} > 26$. The region indicated by heavy lines in the top left is where we expect to find $z \simeq 4$ objects similar to those of Steidel et al. (1999). The light solid lines show the expected evolution of Coleman et al. (1980) galaxy templates, and the dotted lines show the Kinney et al. (1996) SB2 and SB3 galaxy templates. The expected colors of stars from Pickles (1998) are over plotted as stars. The downward facing triangles at $B-R = 6$ are objects that were not detected in B.

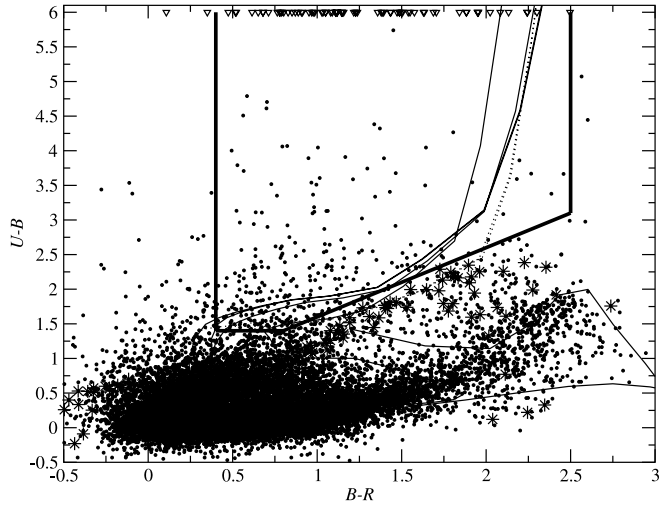

FIG. 21.—$B-R$ vs. $U-B$ color-color plot for all objects with $B_{AB} > 26$. The region indicated by heavy lines in the top right is where we expect to find $z \simeq 3$ objects similar to those of Steidel et al. (1995). The light solid lines show the expected evolution of Coleman et al. (1980) galaxy templates, and the dotted lines the Kinney et al. (1996) SB2 and SB3 galaxy templates. The expected colors of stars from Pickles (1998) are overplotted as stars. The downward facing triangles at $U-B = 6$ are objects that were not detected in U.

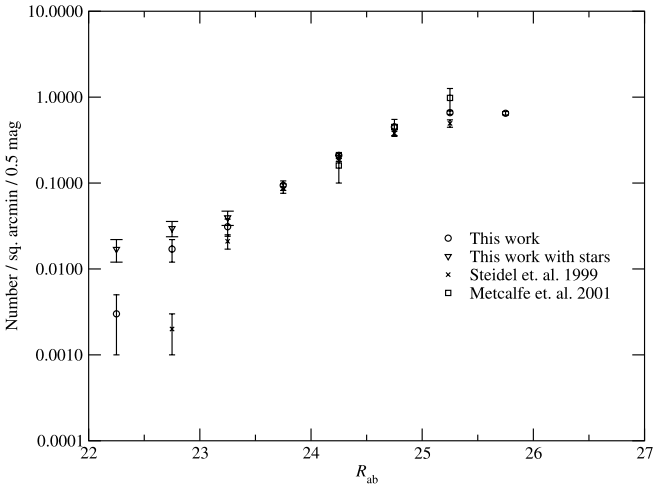

FIG. 22.—Raw sky density of *U*-band dropouts uncorrected for contamination or incompleteness. Error bars are 1 σ Poisson fluctuations for Metcalfe et al. (2001) and our data. The errors for Steidel et al. (1999) include an estimate of cosmic variance from their multiple fields. Much of the variation between the counts is likely due to cosmic variance.

filters, which fall blueward of the Lyman break, between the Lyman break and Lyα line, and redward of Lyα, respectively. Steidel et al. (1999, 1995) successfully use a set of customized filters to select galaxies at $z \simeq 3$ and $z \simeq 4$. Their spectroscopic follow-up has more than 80% success in identifying $z \simeq 3$ galaxies. Metcalfe et al. (2001) has also used these criteria on the Herschel Deep Field and HDF-N.

The number and type of object selected are strongly dependent on the filters and selection criteria used. Changing these parameters can severely effect the success in identifying high-redshift galaxies and change the redshift range selected. For comparison with the previous work, we need to select the same population as Steidel et al. (1999, 1995) and Metcalfe et al. (2001). However, our band passes differ significantly from theirs. We corrected this by calculating the expected colors for the galaxies they have selected. These colors are calculated by integrating the galaxy templates of Coleman et al. (1980) and Kinney et al. (1996) moderated by our filter response profile. We correct these templates for Lyα and Lyβ absorption following the prescription of Madau (1995). We also calculate the expected colors of stars using the spectral library of Pickles (1998). We then set a selection criteria that will select similar galaxies to the previous work, but avoids stars. The resulting selection is shown in Figures 18 and 20, along with color-color tracks for various galaxy types. The selection is also shown along with our data in Figures 19 and 21.

The surface density we measure using this selection is similar to that measured by other authors (Metcalfe et al. 2001; Steidel et al. 1999) (see Figs. 22 and 23 and Tables 11 and 12). Because of our redder *U*-band filter, the $z \simeq 3$ selection suffers more contamination from stars and low-redshift galaxies than that of Steidel et al. (1999, 1995). We attempted to remove stars by selecting objects with $R < 23.5$ and $R_{\rm FWHM} > 1\farcs3$, as described in McCracken et al. (2001); however, the contamination from galaxies remains. At magnitudes fainter than $R = 23$ our measurements are within the 1 σ error bars reported by Steidel et al. (1999, 1995) and Metcalfe et al. (2001). Our *B*-band counts are consistent with but systematically lower than those of Steidel et al. (1999) or Metcalfe et al. (2001), which is likely because of cosmic variance.

The selection at redshifts higher than $z \simeq 4$ is significantly more difficult. The contamination for $z \simeq 3$ galaxies comes from low-redshift galaxies, where the comoving volume is small. For $z > 5$ galaxies, the contamination comes from $z \simeq 1$, where the effective comoving volume is very large. Several authors using color-color selection have recently reported the discovery of large numbers of $z > 5$ galaxies (Iwata et al. 2003; Lehnert & Bremer 2003). However, we find their two-color selection yields a large number of lower redshift galaxies. Figure 17 shows an example for a redshift 5.5 galaxy. Elliptical galaxies at $1 < z < 1.5$ have similar colors to a $z > 5.5$ galaxy in the *R*, *I*, and z' bands. The only clear difference is in the bluer or redder bands. In particular, the use of an $R-I$ selection will include many low-redshift galaxies. A similar problem will occur at redshift 6 using an $I-Z$ selection. There is no easy solution; either one must go more than 3 mag deeper in the bluest band than the reddest or obtain deep near-IR imaging, both of which are time intensive for large surveys.

Songaila et al. (1990) set out a clear criteria for selecting high-redshift galaxies, based on the Lyα absorption shown in equation (2):

$$\Delta m_{\rm Lycont} = 3.8 + 20.3 \log\left(\frac{1+z}{7}\right). \quad (2)$$

For $z > 5$ galaxies, it requires $V-I > 2.4$ and no detection blueward of the 912 Å break. Using these criteria and our multicolor data, we can test the findings of other authors. To test the level of contamination, we have restricted ourselves to $z' > 25$, which is bright enough for the expected contaminating sources to be detected at 2 σ in *U* or *B* bands.

Iwata et al. (2003) imaged the same area with Suprime-Cam in the same *V*, *I*, and z' filter we used. However, they calibrated

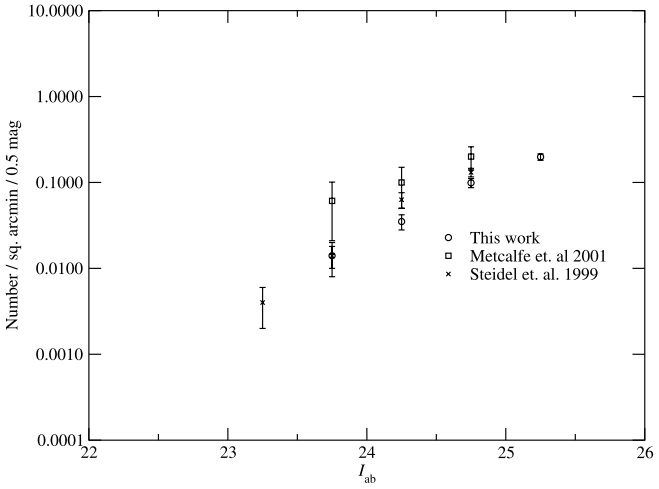

FIG. 23.—Raw sky density of *B*-band dropouts uncorrected for contamination or incompleteness. Error bars are 1 σ Poisson fluctuations for Metcalfe et al. (2001) and our data. The errors for Steidel et al. (1999) include an estimate of cosmic variance from their multiple fields. Much of the variation between the counts is likely due to cosmic variance.

TABLE 11
NUMBER DENSITY OF *U* DROPOUTS

R Magnitude	*N* arcmin^{-2} 0.5 mag^{-1}	With Stars Error	*N* arcmin^{-2} 0.5 mag^{-1}	Without Stars Error
22.25.....	0.017	0.005	0.003	0.002
22.75.....	0.030	0.006	0.017	0.005
23.25.....	0.040	0.007	0.031	0.007
23.75.....	0.095	0.012	0.095	0.012
24.25.....	0.214	0.017	0.214	0.017
24.75.....	0.450	0.025	0.450	0.025
25.25.....	0.661	0.031	0.661	0.031
25.75.....	0.653	0.030	0.653	0.030

TABLE 12
NUMBER DENSITY OF *B* DROPOUTS

I Magnitude	*N* arcmin^{-2} 0.5 mag^{-1}	Error
23.25.....	0.0	...
23.75.....	0.014	0.004
24.25.....	0.035	0.007
24.75.....	0.099	0.011
25.25.....	0.198	0.017

their data in a different manner. We adopted $V-I \geq 2.4$ and $V-I \geq 7(I-z') - 0.2$ as our selection criteria (see Fig. 24). This avoids selecting $z \simeq 1$ galaxies and late-type stars. We find that our counts are consistent with but lower than the values of Iwata et al. (2003) (see Fig. 25 and 26 and Tables 13 and 14). Moving our selection slightly redder in $I-Z$ color, increases the number of objects selected, making our numbers more consistent with Iwata et al. (2003). However, all the additional objects are detected in *U* or *B* band. Even when objects detected in *U* or *B* are removed, many of the remaining objects in the ACS GOODS field morphologically appear to be stars (this will be quantified elsewhere). These results suggest that a combination of $z \simeq 1$ galaxies and late-type stars are contaminating the $z > 5.5$ selection.

Figure 25 shows that the selection criteria of Lehnert & Bremer (2003) is very likely selecting low-redshift galaxies or stars. We find that 95% of the objects selecting using this

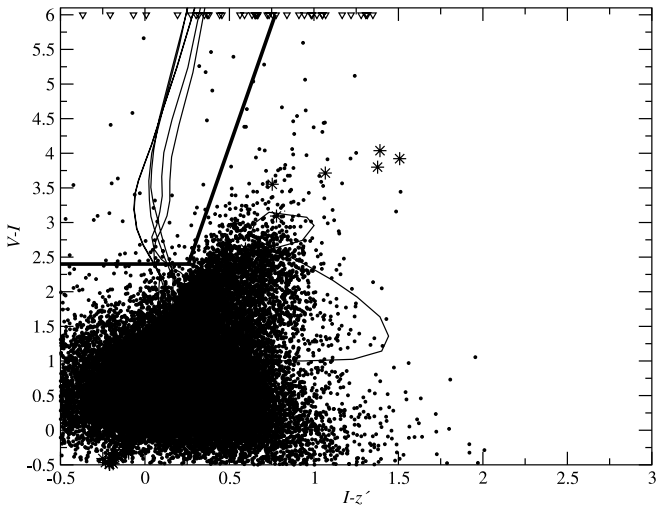

FIG. 24.—$I-z'$ vs. $V-I$ color-color plot for all detected objects. The region indicated by heavy lines in the top left is where we expect to find $z \simeq 5.5$ objects based on the criteria of Iwata et al. (2003). We have moved the cuts to $V-I => 2.4$ and $V-I > 7(I-Z) - 0.2$ to avoid contamination from lower redshift galaxies and late-type stars, as well as account for differences in the photometric system. The expected colors of stars from Pickles (1998) are overplotted as stars. The downward facing triangles at $V-I = 6$ are objects which were not detected in *V*.

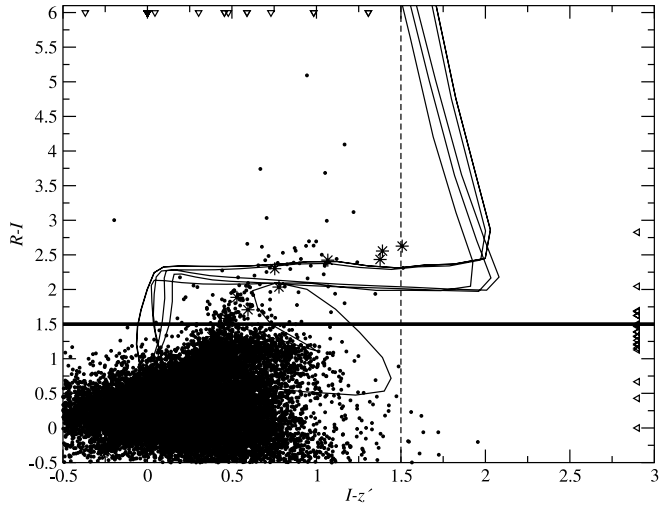

FIG. 25.—$I-z'$ vs. $R-I$ color-color plot for all detected objects. The heavy line at $R-I = 1.5$ indicates the selection criteria of Lehnert & Bremer (2003) and the dashed line at $I-Z = 1.5$ is the selection criteria of Stanway et al. (2003). The light solid lines show the expected evolution of Coleman et al. (1980) galaxy templates and the Kinney et al. (1996) SB2 and SB3 galaxy templates. The expected colors of stars from Pickles (1998) are over plotted as stars. The downward pointing triangles at $R-I = 6$ are objects that were not detected in *R* and leftward pointing triangles at $I-Z = 6$ are objects that were not detected in *I*.

TABLE 13
NUMBER DENSITY OF V DROPOUTS

I Magnitude [a]	N arcmin^{-2} 0.5 mag^{-1}	Error
23.75.....	0.011	0.004
24.25.....	0.019	0.005
24.75.....	0.051	0.008
25.25.....	0.059	0.009
25.75.....	0.061	0.009

[a] $I_c = I - 0.453$ for comparison with Iwata et al. 2003.

TABLE 14
NUMBER DENSITY OF V DROPOUTS NOT DETECTED AT 2 σ IN U OR B WITH $V-I > 2.4$

I Magnitude	N arcmin^{-2} 0.5 mag^{-1}	Error	Percentage of Interlopers
23.75.....	0.001	0.001	90.9
24.25.....	0.010	0.004	47.4
24.75.....	0.038	0.007	25.5
25.25.....	0.047	0.008	20.3

criteria are detected at 2 σ in V. This selection is particularly problematic since it may include star-forming galaxies at $z < 2$, where [O III] or [O II] can be mistaken for Lyα. Finally, the $I-Z > 1.5$ selection used by Stanway et al. (2003) selects objects that are detected at 2 σ in V band 53% of the time. In contrast, only 14% of objects selecting using the $B-R$, $R-I$ selection were detected in U band. Based on our number counts, the probability of an object at 28th magnitude falling into a 3″ aperture by chance is 37% in V band and 4% in U band. This implies that color selection may be overestimating the number of high-redshift galaxies and hence the star formation rates at $z > 5$. We shall give a more extensive discussion of this issue with photometric redshift estimates in a future paper (Capak et al. 2004).

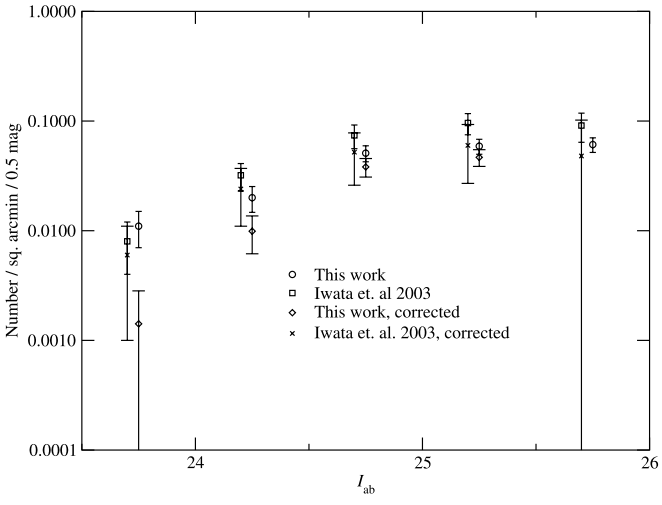

FIG. 26.—Raw sky density of V-band dropouts and an estimate of the density corrected for contamination are shown for the Hawaii-HDF-N. Neither measurement is corrected for incompleteness. Error bars are 1 σ Poisson fluctuations. The counts of Iwata et al. (2003) are higher because of a higher rate of contamination.

3.3. *Conclusion*

We have compiled a deep multicolor catalog over 0.2 deg^2 in the HDF-N region. These data will provide an invaluable basis for understanding the formation and evolution of galaxies by providing a large sample of galaxies that can be studied in various ways. The raw number counts and counts of $z \simeq 3$ and $z \simeq 4$ galaxies agree with those of other authors. However the selection of $z > 5$ galaxies suffers from significant contamination by low-redshift galaxies. The current deep blue imaging is required to reliably select these galaxies and hence estimate the star formation rate.

We would like to thank Nick Kaiser for providing his software and supporting it. We would also like to thank H. McCracken and N. Metcalfe for providing their number count data. The work of C. M. and D. S. was carried out at Jet Propulsion Laboratory, California Institute of Technology, under a contract with NASA. This work was supported by NASA grant DF1-2001X (L. L. C.) and NSF grants AST 00-71208 (E. M. H.), AST 00-84816 (L. L. C.), and AST 99-83783 (A. J. B.).

REFERENCES

Barger, A., Cowie, L., Capak, P., Alexander, D., Bauer, F., Fernandez, E., Garmire, G., Hornschemeier, A., & Brandt, W. 2003, AJ, 126, 632
Barger, A. J., Cowie, L. L., Brandt, W. N., Capak, P., Garmire, G. P., Hornschemeier, A. E., Steffen, A. T., & Wehner, E. H. 2002, AJ, 124, 1839
Benítez, N. 2000, ApJ, 536, 571
Bershady, M. A., Lowenthal, J. D., & Koo, D. C. 1998, ApJ, 505, 50
Bertin, E., & Arnouts, S. 1996, A&AS, 117, 393
Brown, G. S., & Tinsley, B. M. 1974, ApJ, 194, 555
Capak, P., Cowie, L., Hu, E., & Barger, A. 2004, in preparation
Cohen, J. G., Hogg, D. W., Blandford, R., Cowie, L. L., Hu, E., Songaila, A., Shopbell, P., & Richberg, K. 2000, ApJ, 538, 29
Coleman, G. D., Wu, C.-C., & Weedman, D. W. 1980, ApJS, 43, 393
Cowie, L. L. 1988, in Post-Recombination Universe, ed. N. Kaiser & A. N. Lasenby (Dordrecht: Kluwer), 1
Djorgovski, S., et al. 1995, ApJ, 438, L13
Fernández-Soto, A., Lanzetta, K. M., & Yahil, A. 1999, ApJ, 513, 34

Gardner, J. P., Cowie, L. L., & Wainscoat, R. J. 1993, ApJ, 415, L9
Hodapp, K.-W., et al. 1996, NewA, 1, 177
Hu, E. M., Cowie, L. L., McMahon, R. G., Capak, P., Iwamuro, F., Kneib, J.-P., Maihara, T., & Motohara, K. 2002, ApJ, 568, L75
Huang, J.-S., et al. 2001, A&A, 368, 787
Iwata, I., Ohta, K., Tamura, N., Ando, M., Wada, S., Watanabe, C., Akiyama, M., & Aoki, K. 2003, PASJ, 55, 415
Jacoby, G. H., Liang, M., Vaughnn, D., Reed, R., & Armandroff, T. 1998, Proc. SPIE, 3355, 721
Kaiser, N. 2000, ApJ, 537, 555
Kinney, A. L., Calzetti, D., Bohlin, R. C., McQuade, K., Storchi-Bergmann, T., & Schmitt, H. R. 1996, ApJ, 467, 38
Lehnert, M., & Bremer, M. 2003, ApJ, 593, 630
Madau, P. 1995, ApJ, 441, 18
McCracken, H. J., Le Fèvre, O., Brodwin, M., Foucaud, S., Lilly, S. J., Crampton, D., & Mellier, Y. 2001, A&A, 376, 756
Metcalfe, N., Shanks, T., Campos, A., McCracken, H. J., & Fong, R. 2001, MNRAS, 323, 795
Miyazaki, S., et al. 2002, PASJ, 54, 833
Monet, D. B. A., et al. 1998, VizieR Online Data Catalog, 1252, 0
Monet, D. G., et al. 2003, AJ, 125, 984
Moustakas, L. A., Davis, M., Graham, J. R., Silk, J., Peterson, B. A., & Yoshii, Y. 1997, ApJ, 475, 445
Muller, G. P., Reed, R., Armandroff, T., Boroson, T. A., & Jacoby, G. H. 1998, Proc. SPIE, 3355, 577
Pickles, A. J. 1998, PASP, 110, 863
Postman, M., Lauer, T. R., Szapudi, I., & Oegerle, W. 1998, ApJ, 506, 33
Richards, E. A. 2000, ApJ, 533, 611
Saracco, P., Giallongo, E., Cristiani, S., D'Odorico, S., Fontana, A., Iovino, A., Poli, F., & Vanzella, E. 2001, A&A, 375, 1
Soifer, B. T., et al. 1994, ApJ, 420, L1
Songaila, A., Cowie, L. L., & Lilly, S. J. 1990, ApJ, 348, 371
Stanway, E., Bunker, A., & McMahon, R. 2003, MNRAS, 342, 439
Steidel, C. C., Adelberger, K. L., Giavalisco, M., Dickinson, M., & Pettini, M. 1999, ApJ, 519, 1
Steidel, C. C., Giavalisco, M., Dickinson, M., & Adelberger, K. L. 1996, AJ, 112, 352
Steidel, C. C., Pettini, M., & Hamilton, D. 1995, AJ, 110, 2519
Tinsley, B. M. 1972, ApJ, 173, L93
———. 1980, ApJ, 241, 41
Williams, R. E., et al. 1996, AJ, 112, 1335
Wolfe, T., Reed, R., Blouke, M. M., Boroson, T. A., Armandroff, T., & Jacoby, G. H. 1998, Proc. SPIE, 3355, 487
Yasuda, N., et al. 2001, AJ, 122, 1104